



Analysis on mechanical properties and mesoscopic acoustic emission characteristics of prefabricated fracture cemented paste backfill under different loading rates

Xuepeng Song¹ · Quan Yuan¹ · Shi Wang² · Zilin Dong¹ · Yuxin Hao¹

Received: 10 June 2022 / Accepted: 28 October 2022 / Published online: 8 November 2022
© The Author(s), under exclusive licence to Springer-Verlag GmbH Germany, part of Springer Nature 2022

Abstract

The mechanical characteristics of cemented paste backfill (CPB) are significantly influenced by the loading rate (LR) and initial defects. Therefore, the CPB with prefabricated fracture (PF, PFCPB) was prepared, and uniaxial compressive strength (UCS) tests considering LR and acoustic emission (AE) monitoring were performed. The particle flow code (PFC2D) was introduced to analyze the mesoscopic crack evolution of the filling body, and the moment tensor theory was used to invert the AE signals characteristics. The results show that as the PF angle increased, the UCS and elastic modulus (EM) of PFCPB decreased and then increased, and the 30° PF was the turning point. The mechanical properties of PFCPB were deteriorated by the presence of PF. Meanwhile, the mechanical properties of PFCPB were positively correlated with the LR. The stress–strain curve of PFCB (excluding 90°) showed bimodal curves. After the UCS test, the macro crack of PFCPB sprouted at the tip of PF or converged toward PF. PFCPB mainly suffered from shear failure, accompanied by a few tensile failures. Numerical simulation results showed that the crack initiation stress of PFCPB was reduced by the PF. The number of cracks first dropped and then gradually increased when the PF angle was enhanced, while gradually increased with the LR increased. Meanwhile, the mesoscopic AE characteristics of CPB were strongly in line with the test results. The AE events of 0~60° PFCPB experienced two slow rising periods and rapid rising periods. The temporal and spatial distribution characteristics of AE corresponded to the crack evolution trend. The PF was prone to stress concentration, especially at the tip and upper and lower surfaces of 0~45° PF, resulting in rapid crack initiation and reducing the energy storage limit and mechanical behavior of 0~45° PFCPB. The increasing LR (within a certain range) was in favor of improving the mechanical behavior of the filling body. The research results can provide a basic reference for the stability evaluation of the filling body with initial defects.

Keywords Cemented paste backfill · Mechanical properties · Acoustic emission · Prefabricated fracture · Loading rate · Particle flow code

Introduction

The mining industry is the basis of many industries which provides a favorable guarantee for human life and social progress. With the demand and economic growth of social

development, mining activities around the world are increasingly frequent, and the extraction of deep earth resources becomes the new normal (Zhao et al. 2022a, b; Hou et al. 2022; Xie 2019). However, deep mining will inevitably face the complex environment of “three high and one disturbance,” which in turn leads to frequent disasters such as rock-burst and goaf instability, thus seriously hindering the efficiency of resource exploitation and threatening the safety of life and property (Huang et al. 2021; Wu et al. 2020; Kuyuk et al. 2020). Therefore, filling mining may become an effective method for solving the above problems. In recent decades, cemented paste backfill (CPB) has been increasingly applied in underground metal mines because it can dispose of surface tailings, support goaf, and improve ore recovery rate (Fang and Fall 2018; Yilmaz 2018; Tao et al. 2022). The

Responsible Editor: Philippe Garrigues

✉ Xuepeng Song
sxp9612@126.com

¹ School of Energy and Mining Engineering, China University of Mining and Technology (Beijing), Beijing 100083, China

² School of Resources and Environmental Engineering, Jiangxi University of Science and Technology, Ganzhou 341000, China

hardened CPB has the effect of isolating and transferring stresses (Wang et al. 2021a, b; Song et al. 2022a). Therefore, it is of important practical significance to research the mechanical behavior of the CPB for guiding the filling ratio and enhancing the safety of underground working.

However, during the actual filling operation, factors such as stress disturbance in the mining of the deposit, explosion stress wave, flying stone, unfavorable geological formations, and worse filling effects are prone to cause many joints, fractures, and other defects inside filling body (Xu et al. 2018; Hou et al. 2020a). These defects are more prone to stress concentration under external loading, which accelerates the initiation, and propagation of cracks inside the filling body, and even changes the crack propagation form of the filling body, thus degrading the mechanical behavior of the filling body. As a result, the fill may be more susceptible to destabilization damage, threatening the safety of downhole operations and increasing the loss depletion rate of the ore. It is important to emphasize that in the subsequent filling mining method, the stress state of the filling body changes from a three-phase stress state to unloading due to the two-step mining of adjacent ore bodies. With the continuous mining of adjacent ore bodies, the stresses of surrounding rock and backfill are changed, which is reflected in the indoor experiments as the different loading rates (LR) (Hou et al. 2020b). The reasonable LR is determined through indoor experiment, and then the mining speed is converted, which has a certain guiding significance for underground safety production. However, the internal crack evolution law of the filling body with defects may be further changed under the influence of LR, and the stability of the corresponding backfill structure is uncertain. For a long time, domestic and foreign scholars have conducted extensive research on the effects of joints, fractures, and LRs on rock crack propagation and mechanical characteristics. Yu et al. (2021) explored the effect of LR on the crack extension of fractured sandstone through laboratory tests and numerical simulation. Li et al. (2022) performed true triaxial tests on fractured rocks, which identified the crack formation mechanism. Haeri et al. (2014) conducted Brazilian splitting tests on rock-like materials with fractures, and the effects of fracture inclination and number on crack evolution were analyzed. Shirole et al. (2021) investigated the damage process of rock with defects by using a nonlinear ultrasonic testing method and scale subtraction. For the filling body, Xu et al. (2018) analyzed the effects of curing temperature and 45° prefabricated fractures (PF) on the strength and crack expansion pattern of the filling body. Hou et al. (2020a) established the damage variable to describe the filling body with 45° PF under different osmotic pressure through experimental and numerical research.

In summary, on the one hand, there are only a few systematic researches on the strength properties and crack evolution

of the filling body with PF, focusing only on a single dip angle fracture, which is not enough to fully understand the performance changes caused by the change of fracture dip. On the other hand, the effect of LR on the mechanical performance of the filling body cannot be ignored. The rock and backfill generally show a certain LR effect (Cao et al. 2019; Xiu et al. 2021; Cheng et al. 2019). It is worth mentioning that, as an artificial cement-based composite, there is a considerable number of microporous cracks in the filling body. Moreover, the compressive strength of the filling body is greatly below that of the rock and has a certain ductility after failure. The crack propagation and stress–strain behavior of filling body are significantly different from those of rock materials. Therefore, the research results of fractured rock cannot be directly applied to the filling body. As such, it is of great significance to systematically study the mechanical behavior and crack evolution characteristics of the filling body with PF under different LRs.

Moreover, with the development of computer technology, acoustic emission (AE) monitoring and particle flow code (PFC) are increasingly being employed for geotechnical stability monitoring and mesoscopic damage (Wang et al. 2022a, b; Ma et al. 2020; Khazaei et al. 2015; Harizi et al. 2022; Xue et al. 2023). AE signals are strongly correlated with the internal damage evolution of materials during loading. By monitoring the AE signal of material in the whole process loading, the crack propagation process in the filling body can be inverted according to the obtained AE parameters and the moment tensor theory, and the location of crack and fracture can be determined (Zhao et al. 2020a, b; He et al. 2021). Generally, AE source location requires many AE probes (6–8 probes) to be mounted on the surface of the sample to obtain AE information. It may lead to the difference between the gained moment tensor and the realized cases due to factors including the arrangement mode and number of AE probes, the contact degree with the surface of the sample, the presence of external disturbances, and the difference in sample size and homogeneity (Mondoringin and Ohtsu 2013; Zhang et al. 2020; Cheng et al. 2021). The accurate acquisition of moment tensor through indoor experiments is still a hot topic in recent years. At the mesoscopic level, the PFC can discrete the specimens into particles of different sizes, and the mesoscopic characteristics of materials can be accurately obtained by referring to macroscopic tests to calibrate the mesoscopic parameters between the particles. More importantly, the mesoscopic AE characteristics of the material can also be accurately obtained by introducing the moment tensor theory, and the method is not limited by the above factors.

In view of the above problems, in this study, the UCS test of CPB and PFCPB was firstly carried out, the relationship between PF angle, LR and UCS, EM was quantified, the stress–strain behavior of the filling body was discussed, and

the failure features of the filling body were explored. Then, the effects of PF angle and LR on the mesoscopic crack evolution of the filling body were analyzed by using PFC2D. On this basis, the development law and temporal and spatial distribution (TSD) characteristics of AE events were studied by using the moment tensor theory. Finally, with the help of energy conservation theory, the mechanism of PF angle and LR on the change of mechanical behavior of the filling body was further discussed.

Materials and methods

Raw materials

The raw materials used in this experiment include tailings, cement, and water. Among them: ① the tailings are taken from a copper mine in Jiujiang City, Jiangxi Province. The laser particle sizer and X-ray fluorescence spectrum analyzer were used to analyze the particle size distribution and chemical composition of the tailing. The test results are shown in Fig. 1 and Table 1, respectively. As shown in Fig. 1, the particle size of the tailings used in the experiment is medium-fine, and the particle grading is good (Song et al. 2022a). Moreover, the tailings are mainly composed of SiO₂ and CaO, which are favorable to the strength development of the filling body. ② The binder is the main source for obtaining the strength of CPB. The cementitious agent is P.O 42.5 cement frequently employed in mines. ③ The mixed water is laboratory tap water.

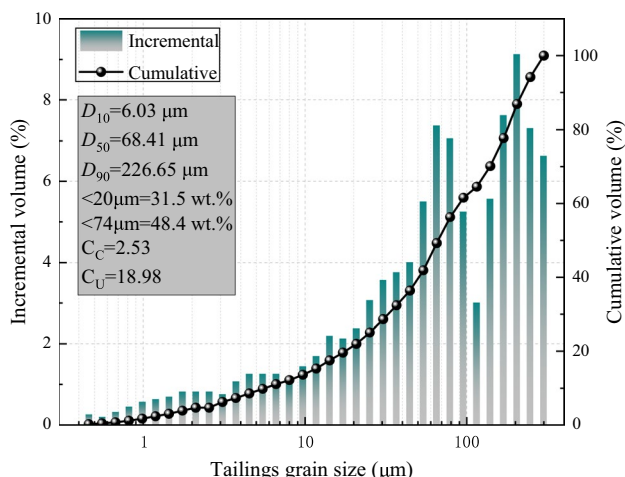


Fig. 1 Particle size distribution of the tailings

Table 1 Chemical composition of the tailings

Composition	SiO ₂	CaO	Fe ₂ O ₃	SO ₃	Al ₂ O ₃	MgO	K ₂ O	Na ₂ O	MnO	TiO ₂	P ₂ O ₅	Others
Content /%	31.879	23.466	15.520	9.881	5.615	4.451	0.402	0.259	0.223	0.184	0.149	7.971

Experiment methods and numerical simulation

In this paper, the experiment and numerical simulation mainly include preparation of the filling body, UCS tests under different LRs with AE monitoring, the establishment of mesoscopic model, and AE characteristic inversion based on moment tensor theory. The research steps are shown in Fig. 2.

The filling body preparation

The preparation steps of the filling body are as follows: ① The unclassified tailings collected in the mine were dried to constant weight at the temperature of 50 °C in the drying oven, and then a certain amount of tailings was weighed and fully mixed with cement in a JJ-5 mixer. ② Before the experiment, the bottom center of the cube mold (70.7 mm) was prepared with different-angled grooves. A top cover of the cube mold was prepared, and the opening corresponding to the bottom was prefabricated at the center of the top cover. Then, the fresh paste was poured into the mold, and an iron sheet coated with lubricating oil is inserted into the groove at the bottom of the mold from top to bottom through the opening of the top cover, ensuring that the iron sheet is always upright. ③ After 24 h, all specimens are demolded and the iron sheet for performing the PF is pulled out in the filling specimen. Then, the filling sample was cured for 28 days (relative humidity is 90 ± 2% RH, and temperature is 20 °C). The specific experimental protocols are shown in Table 2.

UCS tests under different LRs and AE signals monitoring

The UCS tests with different LRs are carried out on CPB and FCPB specimens using an electronic universal press (According to GB/T50123–2019). Refer to the research of Hou et al. (2020b), Xiu et al. (2021); Gan et al. (2016), the LRs in this paper are 0.1, 0.25, 0.5, 1, and 2 mm/min, respectively. The UCS tests and AE monitoring steps are as follows (Zhao et al. 2020a, b; He et al. 2021): ① The filling body sample is placed at the loading end of the press, the displacement loading mode is selected, and the stress and strain data are automatically recorded in the whole loading process. ② With the help of the PC-II AE monitoring system, UT 1000 (working frequency: 60–1000 kHz) and R6 (working frequency: 35–100 kHz) AE probes are selected, and the noise threshold is 45 dB. The UCS tests are carried out simultaneously with AE monitoring.

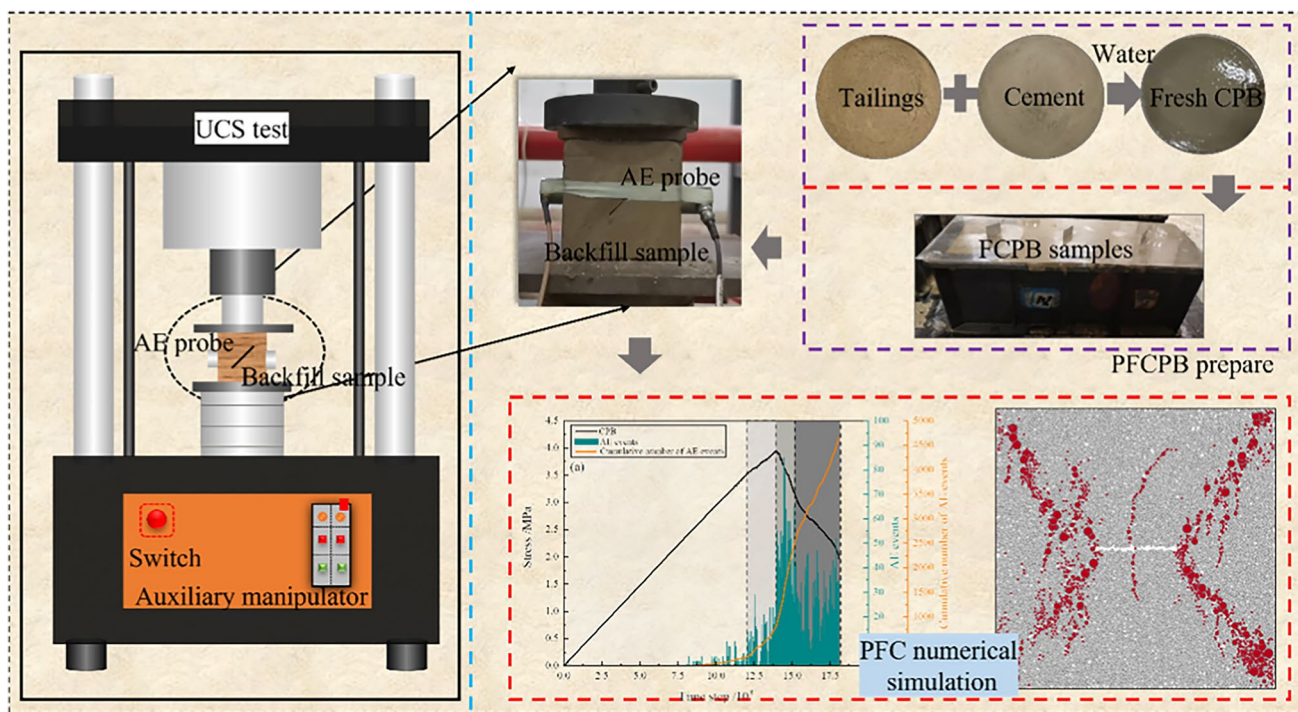


Fig. 2 Research steps

Table 2 Test scheme

No	Mass ratio of cement to tailings	Mass concentration /%	PF angle /°	LR /(mm/min)	Curing age
C	1:4	76	-	0.1, 0.25, 0.5, 1, 2	28 d
C-0			0		
C-30			30		
C-45			45		
C-60			60		
C-90			90		

Mesoscopic model of CPB and PFCPB establishment

Particle flow code abstracts rock, concrete, filling body, and other material media into discrete particles as a special discrete element method. The numerical simulation of material macro mechanical behavior and mesoscopic structure can be realized by defining parameters between particles (Xin 2020). The CPB is a kind of cement-based composite material, and its strength is mainly derived from cement hydration. In this paper, the failure process of the filling body under UCS tests is simulated based on PFC2D. Firstly, a two-dimensional model completely consistent with the size of CPB is generated. The model consists of particles and is constrained by the wall. After the model is generated, the side wall is deleted, and the LR is controlled by the upper

and lower walls, which is the same as the physical test. Thereafter, AutoCAD software is used to import walls with different angles (20 mm long and 0.5 mm wide), and the PF is generated by deleting particles within the size range. Finally, according to the experimental results, the ‘trial and error method’ is used to calibrate the mesoscopic parameters of the mesoscopic model by using the parallel bonding model. The specific parameter calibration method can be referred to in the literature published by Yu et al. (2021). The experimental and numerical simulation results are shown in Fig. 3.

AE feature inversion based on moment tensor

During the uniaxial compression simulation, the contact between particles breaks and microcracks occurs, and the released strain energy is partially transformed into seismic waves, i.e., AE events (Sun and Wu 2021).

In the study of earthquake source mechanisms, moment tensor theory is commonly utilized in the field of rock and concrete (Cheng et al. 2021; Hu et al. 2021). In this paper, the moment tensor theory is introduced to statistic the magnitude and source of AE events of CPB and PFCPB under different LRs. During the numerical simulation of PFC, the two contact particles that are locally or partially endowed with parallel bonding model due to the applied external load sprout microcracks and the two particles that sprout microcracks are considered source particles (Sun and Wu 2021;

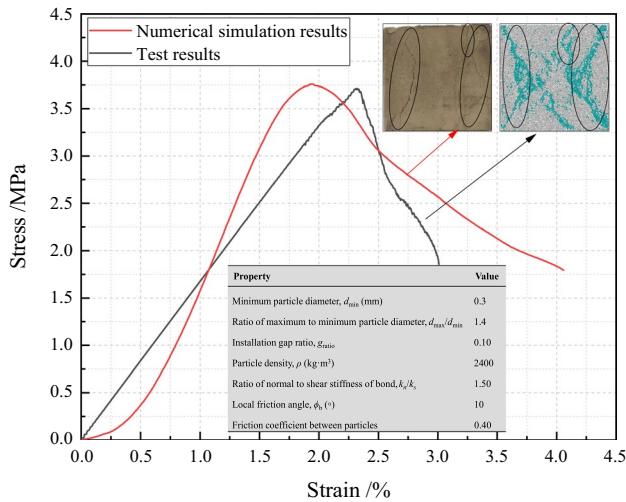


Fig. 3 Comparison of results and mesoscopic parameters

Cheng et al. 2021; Hu et al. 2021). Meanwhile, the source particles also move relative to each other while sprouting microcracks, resulting in the displacement of the contact, which in turn causes a change in the contact force, and the generation of microcracks is considered an AE event (Hu et al. 2021; Zhao et al. 2021). The AE moment tensor M_{ij} can be obtained by multiplying the variation of the contact force in parallel bonded contact by its corresponding force arm and summing, and its calculation formula is as follows:

$$M_{ij} = \sum_s (\Delta F_i R_j) \tag{1}$$

where ΔF_i is the i th component of the change in interparticle contact force; R_j is the j th component of the distance between the contact point and the center of the microcrack.

According to M_{ij} , the scalar moment M_0 (Cheng et al. 2021):

$$M_0 = \left(\frac{\sum_j^3 m_j^2}{2} \right)^{1/2} \tag{2}$$

where m_j is the j th characteristic in the moment tensor matrix.

The rupture intensity of AE events can be characterized by magnitude, which represents the size of fault surface misalignment and released energy caused by AE events. The magnitude M can be calculated based on the maximum value of the scalar moment (Cheng et al. 2021):

$$M = \frac{2}{3} \log M_0 - 6 \tag{3}$$

Results and analysis

Evolution of UCS of CPB and PFCPB

The influence of PF angle and LR on the evolution law of UCS of the filling body is shown in Fig. 4. Detailed discussion will be made below.

The effect of PF angle

Figure 4a illustrates the relationship between UCS and PF angles. From Fig. 4a, it is clear that with the increasing PF angle, the UCS of the filling body first diminished and then gradually enhanced, and the 30° PF was the turning point. Take the LR of 0.1 and 1 mm/min as an example. The UCS of the filling body decreased from 2.70 and 3.24 MPa at 0° to 2.42 and 3.03 MPa at 30° and decreased by 10.37 and 6.48% respectively and then increased to 3.00 and 3.74 MPa at 90° and increased by 23.97 and 23.43% respectively compared with that of the 30° PFCPB. This phenomenon indicates that the variation of PF angles significantly affects the UCS development of the filling body and can be expressed using cubic polynomials (R^2 is above 0.860, as shown in Eq. (4)). This phenomenon is consistent with the results of the literature (Lu et al. 2021; Song et al. 2022b). Moreover, the UCS of CPB was commonly greater than that of PFCPB at the same LR, i.e., the strength characteristics of the filling body were deteriorated by the presence of PF. The deterioration degree can be obtained according to Eq. (5) and the results are plotted in Fig. 4c. It is obvious from Fig. 4c that the effect of PF angle on the degradation degree of UCS of the filling body was opposite to the trend of UCS, and the degradation degree reached the maximum at 30°. These phenomena are explained as follows: (1) The existence of PF is equivalent to the arrangement of initial defects inside the filling body, and the location of PF under external loading is more likely to have stress concentration, which is conducive to the sprouting, and development of cracks inside the filling body. Faster crack evolution rate before the peak stress results in reduced load-carrying capacity of the filling body and reduced UCS. (2) The stress concentration at the PF tip and the upper and lower surfaces of the 0~45° PFCPB is increased, which is more conducive to crack initiation (which will be discussed in detail in the “The mesoscopic characteristics of CPB and PFCPB” section).

$$\sigma = m_1 + n_1 a + p_1 a^2 + q_1 a^3 \tag{4}$$

where σ is the UCS of PFCPB, MPa; a is the PF angle (0~90°); m_1 , n_1 , p_1 , and q_1 are the parameters related to PF angle and LR respectively.

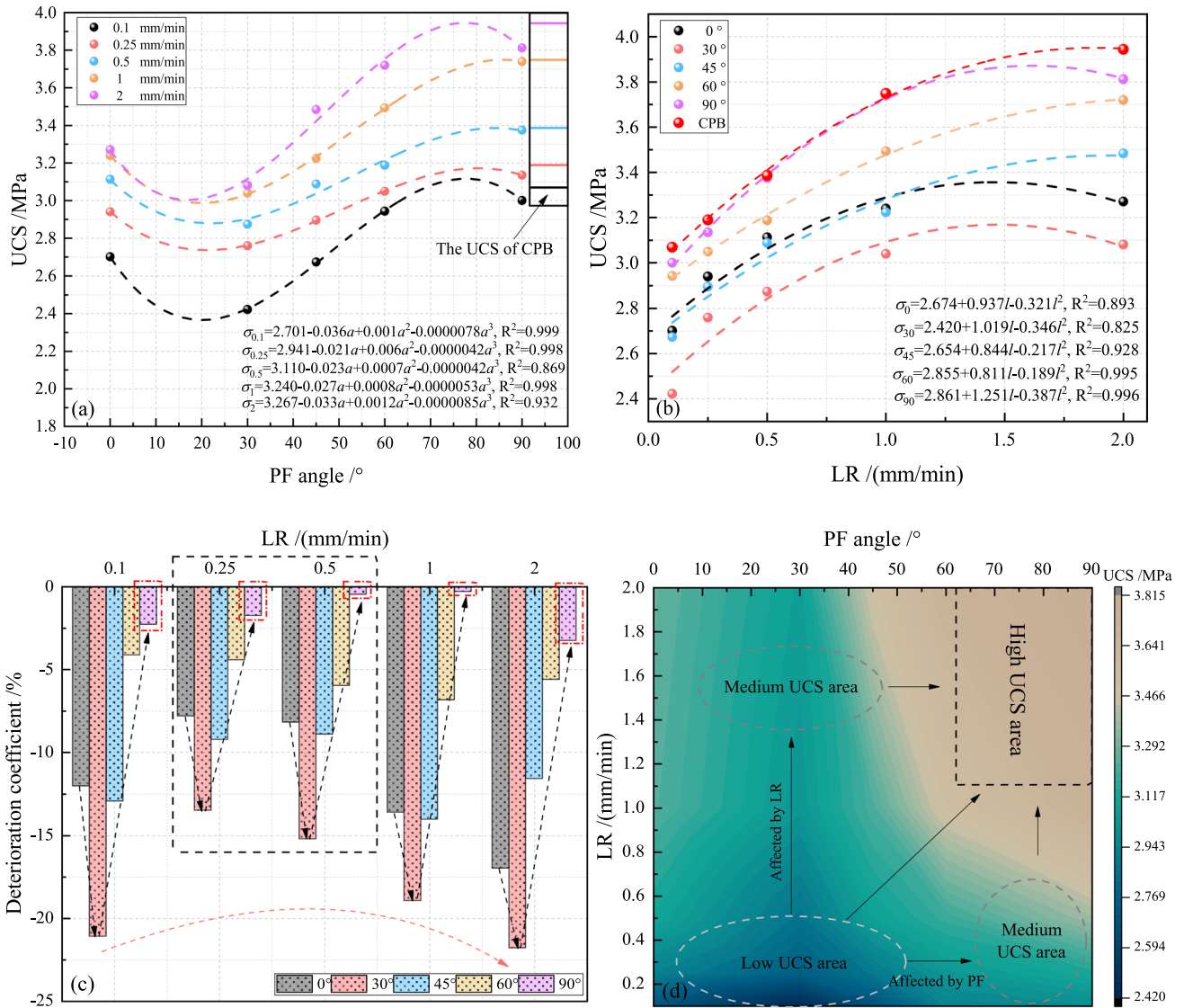


Fig. 4 Effect of PF angle and LR on UCS of the filling body

$$D_{UCS} = \frac{S_{PFCPB}}{S_{CPB}} \quad (5)$$

where D_{UCS} is the deterioration coefficient of UCS, %. S_{PFCPB} and S_{CPB} are the UCS of PFCPB and CPB respectively, MPa.

The effect of LR

Figure 4b illustrates the relationship between the UCS of the filling body and LR. As can be seen from Fig. 4b, when the LR extended from 0.1 to 2 mm/min, the UCS of CPB and PFCPB continued to increase, and the increase rate gradually decreased. The UCS of CPB and 30° PFCPB increased from 3.07 and 2.42 MPa at 0.1 mm/min LR to 3.94 and 3.08 MPa at 2 mm/min LR, respectively,

which increased by 28.34 and 27.27% respectively. This phenomenon indicates that higher LRs (within the appropriate LR range) are beneficial to the enhancement of UCS of the filling body. Meanwhile, it can be clearly found that the UCS of CPB was commonly stronger than that of PFCPB regardless of LR. Among them, the UCS of the 90° PFCPB was close to CPB, indicating that the deterioration degree of 90° PF to the filling body is low, which can also be proved in the deterioration degree diagram shown in Fig. 4c. Overall, the 90° PF had the least effect on the strength properties of the filling body (red dashed line in Fig. 4c), while the LR in the range of 0.25 to 0.5 mm/min (black dashed line in Fig. 4c) could slow down the degradation of PF on the strength of the filling body. These phenomena are explained as follows: (1) Increasing the LR corresponds to an increase in the total

energy exerted by the external load on the filling body (Tang et al. 2022), forcing the filling body with lower energy dissipation to consume the externally applied by lifting its own stress. Therefore, the UCS of the filling body increases with the increase of LR. (2) Higher LR has a certain inhibitory effect on crack development (Gan et al. 2016), which can appropriately improve its own energy storage limit and reduce the crack initiation and propagation caused by energy dissipation, which is beneficial to the strength enhancement of the filling body. These phenomena are similar to the research results of Xiu et al (2021). However, Hou et al (2020b) found that the UCS of the filling body enhanced and then reduced with an increase of LR, and there existed a critical LR. It seems to be different from the results in this paper. This is because the determination of the critical LR is limited by the performance of the filling body, such as the selected concentration, cement content, tailing particle size distribution, and other factors when preparing the filling body. The changes in these factors inevitably lead to changes in the internal pore structure and the ability to resist the external load of the filling body. Therefore, the critical LR is different. This can also be confirmed by the different critical LRs obtained in the studies of Hou et al. (2020b) and Gan et al. (2016). Moreover, according to the results of this paper, the relationship between UCS and LR is quadratic polynomial (such as Eq. (6), $R^2 > 0.82$).

$$\sigma = m_2 + n_2l + p_2l^2 \quad (6)$$

where l is the LR (0.1 ~ 2 mm/min), mm/min; m_2 , n_2 , and p_2 are the parameters related to PF angle and LR respectively.

Coupling effect of PF angle and LR

Figure 4d shows the UCS distribution of the filling body under the coupling action of PF angle and LR. From Fig. 4d, the UCS of the filling body can be divided into low strength area, medium strength area, and high strength area. The main features are as follows: The low strength area was located at the lower left. At this time, the PF angle was between 0 and 45° and the LR was between 0 and 0.5 mm/min. The UCS of PFCPB in this angle range was generally low and insensitive to low LRs. (2) The two medium strength areas were located in the upper left and lower right, respectively. It can be found that the UCS in the upper left area was more sensitive to the high LRs (1 ~ 2 mm/min). However, the PF angles (60 ~ 90°) in the lower right area showed the low LR effect. (3) The high strength area was located in the upper right, corresponding to relatively high LR and large PF angle. The UCS evolution of the filling body at this time had a high sensitivity to both of these factors.

Evolution of EM of CPB and PFCPB

The effect of PF angle

The effect of PF angle on the EM of the filling body is shown in Fig. 5a. From the Fig. 5a, it can be found that the evolution of EM of the filling body with PF was consistent with UCS, and they had a cubic polynomial relationship ($R^2 > 0.830$, which can be expressed by Eq. (7)). Taking the LRs of 0.1 and 1 mm/min as examples, the EM of the filling body decreased from 113.28 and 118.00 MPa at 0° to 107.33 and 112.44 MPa at 30°, respectively, and decreased by 5.25 and 4.71% respectively. Subsequently, the EM gradually increased to 120.04 and 154.49 MPa at 90°, which were 11.84% and 37.40% higher than that at 30° PFCPB. Meanwhile, it can be seen from Fig. 5a that the EM of PFCPB was generally lower than that of CPB, indicating that the presence of PF reduces the stiffness of the filling body, and the deterioration coefficient can be obtained by Eq. (8), and the results are shown in Fig. 5c. From Fig. 5c, when the LR was constant, the deterioration coefficient of EM of the filling body enhanced and then dropped. The 30° PF had the severest deterioration on EM, and the 90° PF had the least effect on the stiffness of the filling body. These phenomena are explained as follows: (1) The existence of PF is equivalent to the arrangement of initial defects in the filling body. Under external load, the PF is easy to produce stress concentration. Compared with CPB, the ability to resist crack initiation and propagation is reduced, and the stiffness of PFCPB is weakened. (2) As mentioned before, the stress concentration in the PF at some angles is greater and the ability of the filling body to resist deformation is further reduced.

$$E = m_3 + n_3a + p_3a^2 + q_3a^3 \quad (7)$$

where E is the EM of the filling body, MPa; m_3 , n_3 , p_3 , and q_3 are the parameters related to PF angle and LR, respectively.

$$D_{EM} = \frac{E_{FPCPB}}{E_{CPB}} \quad (8)$$

where D_{EM} is the deterioration coefficient of EM, %. E_{FPCPB} and E_{CPB} are the UCS of PFCPB and CPB, respectively, MPa.

The effect of LR

Figure 5b illustrates the relationship between EM and LR. As can be seen from Fig. 5b, when the PF angles were between 0 and 45°, with the LR increasing from 0.1 to 2 mm/min, the EM of the filling body fluctuated in a certain range with small changed and an overall increasing trend. The EM of PFCPB (60 ~ 90°) and CPB increased with the increase of LR. When

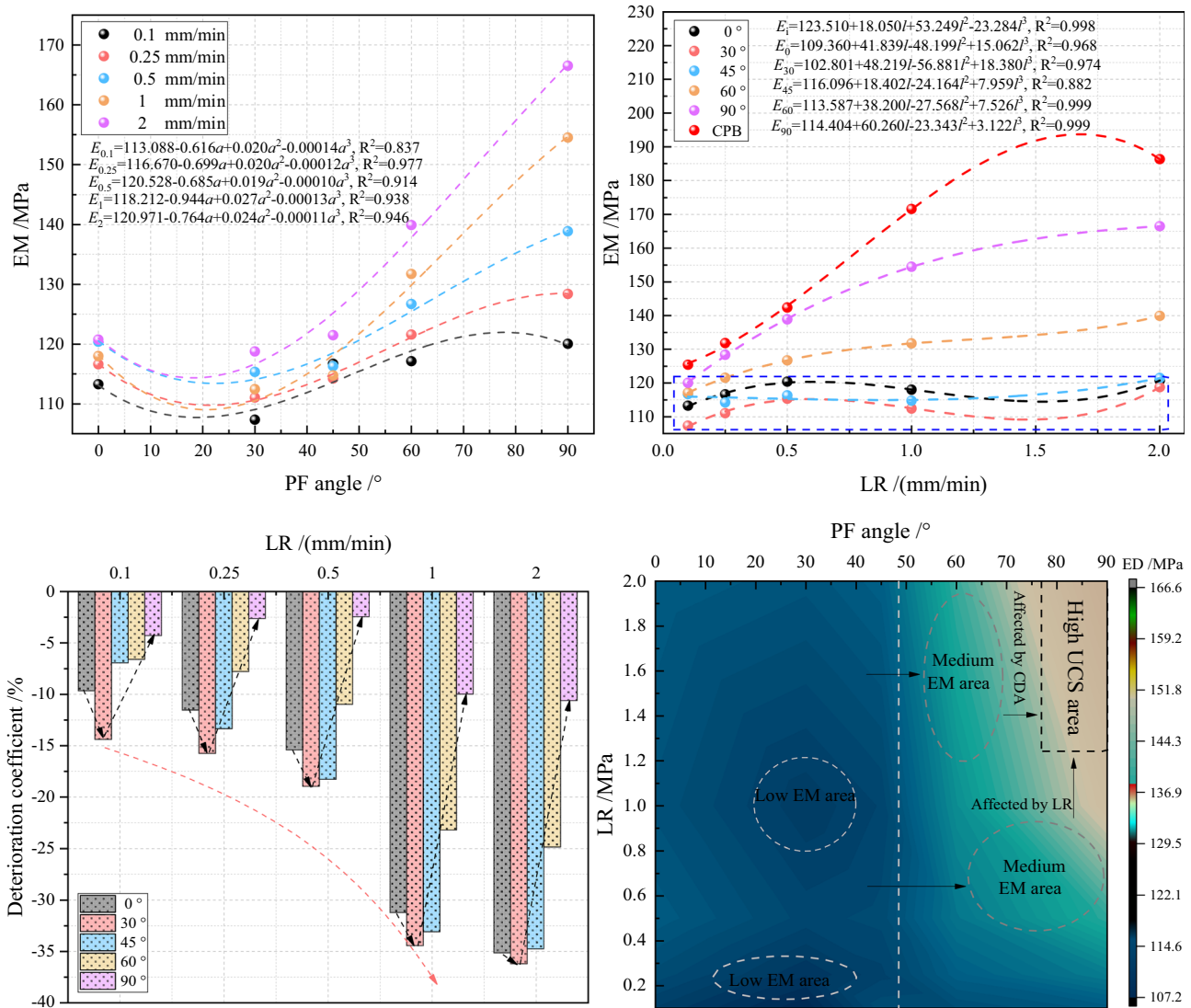


Fig. 5 Effect of PF angle and LR on EM of the filling body

the LR was 0.1 mm/min, the EM of 60°, 90° PFCPB and CPB were 117.12, 120.04, and 125.41 MPa, respectively, and gradually increased to 139.92, 166.52, and 186.32 MPa at 2 mm/min, which were 19.47, 38.72, and 48.57% higher, respectively. The relationship between EM and LR can be expressed in Eq. (9) ($R^2 > 0.880$), and EM can be evaluated by Eq. (9). These phenomena are explained as follows: (1) As described in the “Evolution of UCS of CPB and PFCPB” section, the higher LRs exert higher input energy on the filling body, and higher LRs are conducive to inhibiting the development of cracks, thus inducing the filling body to obtain a higher energy storage capacity and improve its own stiffness. The 0~45° PFCPBs are more likely to sprout cracks at the PF by external loading, resulting in the effect of higher LRs on the hindering effect of internal crack development in the filling body being weakened,

and the LR effect was not obvious in the elastic deformation stage. Furthermore, it can be obtained from Fig. 5c that the deterioration coefficient of EM increased overall with the increase of LR, which might be due to the more significant increase of EM with LR for CPB and the more obvious LR effect (Fig. 5b).

$$E = m_4 + n_4l + p_4l^2 + q_4l^3 \tag{9}$$

where m_4 , n_4 , p_4 , and q_4 are the parameters related to PF angle and LR respectively.

Coupling effect of PF angle and LR

Figure 5d shows the distribution of EM under the influence of the coupling of the two factors. As shown in Fig. 5d, the

EM can be divided into low EM area, medium EM area, and high EM area. The specific distribution characteristics are as follows: (1) The low EM area was located on the left side of Fig. 5d, and PF angles were between 0 and 45°. The EM in this area was generally low and insensitive to the change of LR. (2) The middle EM area was located in the upper right of Fig. 5 as well as being located on the upper right side. When the LR was low (0.1~0.5 mm/min), the EM of 90° PFCPB was more sensitive to low LR, and the sensitivity of 60° PFCPB to LR increased slightly. The sensitivity of the EM of the 60° PFCPB to LR was further increased when the LR was in the range of 0.5 to 1 mm/min. (3) The high EM area was only in a small area in the upper right, and the sensitivity of EM to 90° PF and high LR was the highest, which was further evidence of the high sensitivity of CPB to LR.

Stress–strain characteristics of the filling body

The deformation–damage–instability characteristics of geotechnical materials during the whole process of loading can be completely represented from the stress–strain curve, and the form of the stress–strain curve corresponds to the crack propagation. Stress–strain curves of the filling body at 0.1 and 1 mm/min LR are shown in Fig. 6, respectively. Overall, the development of stress–strain curve went through four stages: initial compaction, elastic deformation, plastic yield, and failure stages. However, there were still some differences in the each phase of curve, especially for PFCPB specimens, which mainly showed the following characteristics:

The form of the stress–strain curves of the filling body (90° PFCPB and CPB) was very similar regardless of LR. This is in line with previous studies (Song et al. 2020b). This phenomenon further indicates that the 90° PF is less

perturbing to mechanics behavior of the filling body, which is also confirmed by previous research results (Song et al. 2020b).

At low LR (Fig. 6a): (1) The stress–strain curve of 0~45° PFCPB first appeared as a slowly growing platform, and then the load was gradually elevated to the peak stress. (2) The curve of 60° PFCPB showed a minor decline in stress after the peak, followed by another increase. These results are attributed to the fact that the PF closed before the peak stress, leading to the phenomenon of stress drop under the larger external load. Continuing to apply the load, the particles on the top and bottom surfaces of PF intrude into mutual, and the degree of mutual engagement (friction) is strengthened (Xu et al. 2018; Song et al. 2022a, b), which strengthen mechanical properties of the filling body. However, the existence of a stress plateau in the curve of stress–strain when PF was between 0 and 45° was due to such PFs being more prone to stress concentration inside the filling body. Therefore, the sprouting and expansion of cracks were advanced, leading to the continued discharge of stored energy inside the filling body and the closure of PF before the peak occurs. When the PF angle was 60°, the UCS and EM of the 60° PFCPB increased, indicating that the sprouting and expansion rate of cracks internal the filling body is lower than the former. Before the peak stress, energy is stored mainly in the form of elastic energy. Thereafter, the upper and lower surfaces of PF might closed rapidly, which led to a significant decline in stress.

At high LR (Fig. 6b): The stress drop of the stress–strain curve in PFCPB (except for the 90° PFCPB) was remarkable. This is because the higher LR exerts higher energy on the filling body, while considering the blocking effect of the high LR on crack propagation, resulting in less energy

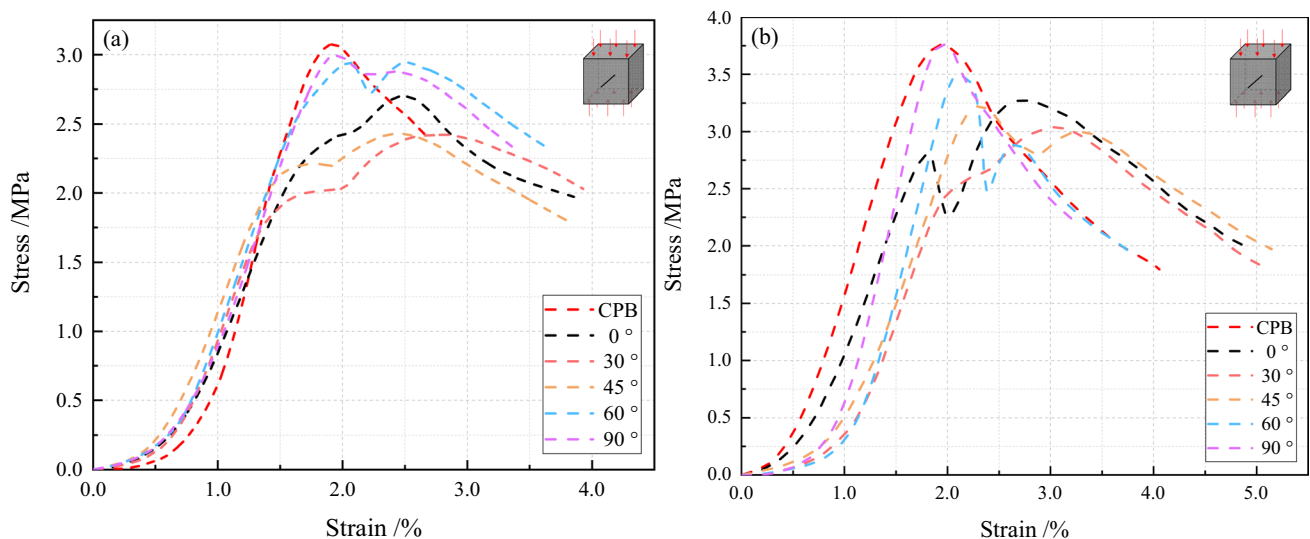


Fig. 6 Stress–strain curve of the filling body (a 0.1 mm/min; b 1 mm/min)

consumption before the peak stress. Near the peak, the energy inside the filling body is rapidly released, the upper and lower part of PF is accelerated to close, and the stress is rapidly reduced. Moreover, the stress–strain curve of 30° PFCPB did not fluctuate greatly. This is because the blocking effect of high LR on the crack propagation of 30° PFCPB is not obvious. The internal cracks of the filling body continue to sprout and propagate during loading, the PF gradually tend to close, and the accumulated elastic strain energy inside is continuously released. The stress–strain behavior of PFCPB is similar to the previous research results (Xu et al. 2018; Song et al. 2022b).

Failure mode of CPB and PFCPB

Geotechnical materials gradually accumulate energy under external load and dissipate energy in the form of crack sprouting and expansion. Eventually, the crack development is complete and the dissipation energy reaches its maximum, and the material undergoes macroscopic damage (Wang

et al. 2021a, b; Zhao et al. 2020a, b). The failure mode of geotechnical material is closely related to the type of crack. Understanding the crack distribution type is the basis for judging the failure mode of geotechnical materials. The types of cracks produced in geotechnical materials under uniaxial compressive loading are shown in Fig. 7, among them, with the wing and secondary cracks being tensile and shear cracks, respectively (Yu et al. 2021). The failure mode of the filling body under typical PF angle (45°) and LR (1 mm/min) will be discussed below.

For PF angle (Fig. 8): Two main shear cracks were penetrating the CPB, leading to shear failure. However, the cracks in PFCPB mainly propagated around the PF, for example, the presence of six types of cracks a, b, c, d, e, and f at the tip of the 0° PF, respectively. There were three types of cracks a, c, and f at the tip of 30° PF, and c and d types of cracks sprout respectively above and below the PF. There were only two types of cracks c and f at the tip of 45° PF, and c-type cracks appeared on the upper end face of the PF. There are mainly three types of cracks c, d, and f at the tip of 60° PF, while there is only one tensile crack at the tip of 90° PF, and the cracks are mainly concentrated on both sides of the PF. Moreover, the crack generated by the PF tip gradually expanded and converged with the far-field cracks to form macro failure.

For LR (Fig. 9): As the LR increased, the cracks in the 45° PFCPB still predominantly extend outward from the PF tip or the top and bottom of the PF. Overall, three main types of cracks c, d, and f were present at the PF tip. Furthermore, when the LR was raised from 0.1 to 2 mm/min, there was no apparent difference in the complexity and evolution mode of cracks in PFCPB. The variation of LR may change the crack initiation stress as well as the rate of crack sprouting, extension and propagation of the filling body. This will be discussed in the numerical simulation section. The crack propagation forms of PFCPB after failure are complex and

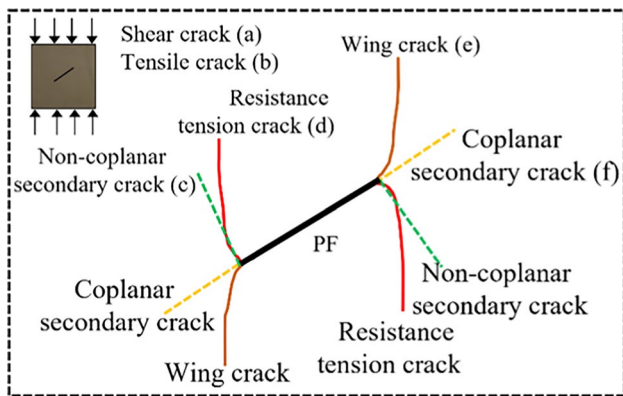


Fig. 7 Crack distribution type

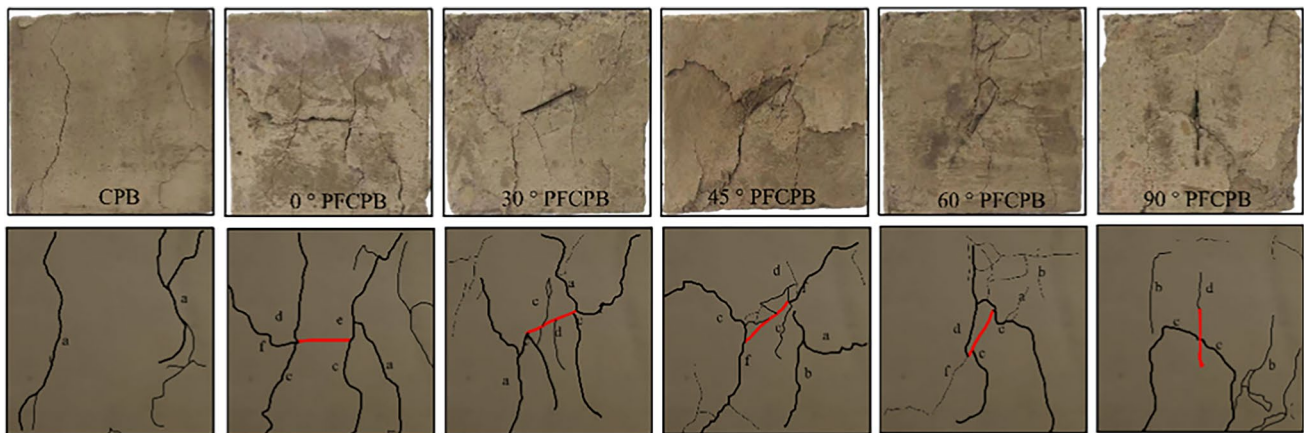


Fig. 8 Failure mode of the filling body (the effect of PF)

diverse, which is markedly distinct from the forms of the crack evolution of hard and brittle materials such as rock obtained in (Yu et al. 2021; Shimbo et al. 2022; Huang et al. 2022; Cao et al. 2016). This is because of the large amount of micropores being dispersed in the filling body, the strength and stiffness of the filling body are low, and the law of crack evolution is weakened, resulting in the complexity of cracks after macro failure.

The mesoscopic characteristics of CPB and PFCPB

Mesoscopic crack evolution of the filling body

The effect of PF angle

The effect of PF angle on the crack expansion pattern of the filling body under the LR of 1 mm/min is shown in Figs. 10, 11, and 12. As shown in Fig. 10a, the stress–strain curve gained by numerical simulation had no initial compaction stage and showed linear elastic deformation behavior. This is because the parallel bonding model has no initial defects, which is different from CPB of artificial cement-based materials. Meanwhile, it can be found that obvious fluctuations could be observed near the peak value, which corresponded to large damage in the filling body. Moreover, when the PF angle enhanced from 0 to 90°, the EM of the filling body reduced and then improved, and it was generally lower than that of CPB. This phenomenon corresponded to the experimental results.

The crack initiation stress, the crack number, and the percentage of pre-peak and post-peak cracks of the filling body for the whole process of loading are presented in Fig. 10a–d. As shown in Fig. 10a, there was no crack initiation in the filling body in the early stage of loading. Subsequently, the crack initiation and slow propagation gradually entered the stage of rapid initiation, expansion, and convergence to failure. The crack number–strain curve was dramatically influenced by the PF angle, which showed the difference between crack initiation stress and crack number. From Fig. 10b–c, the crack initiation stress and cracks number of filling body both reduced and then improved. These phenomena indicate that stress concentration is easily formed around PF, and the sprouting and expansion of cracks inside the filling body are accelerated, followed by worsening of the mechanical properties of the filling body. However, the change trend of the crack number may contradict the characteristics of UCS and EM of PFCPB. These phenomena can be attributed to the following: the filling body is in the state of energy storage and release during the whole process of loading (Wang et al. 2021a, b; Zhao et al. 2020a, b). Energy storage is dominant before the peak stress, accompanied by energy dissipation during crack propagation. After the peak stress, the energy is dissipated rapidly, and the number of crack initiation and propagation is increased. The filling body with higher mechanical properties stores more energy before the peak, resulting in rapid energy released in the post-peak phase and accelerating crack initiation and expansion. Meanwhile, the filling body with lower mechanical properties has lower energy storage limit before the peak due to low crack initiation stress (this process is accompanied by more crack formation and expansion, which increases energy dissipation), resulting in less significant energy release in the post-peak

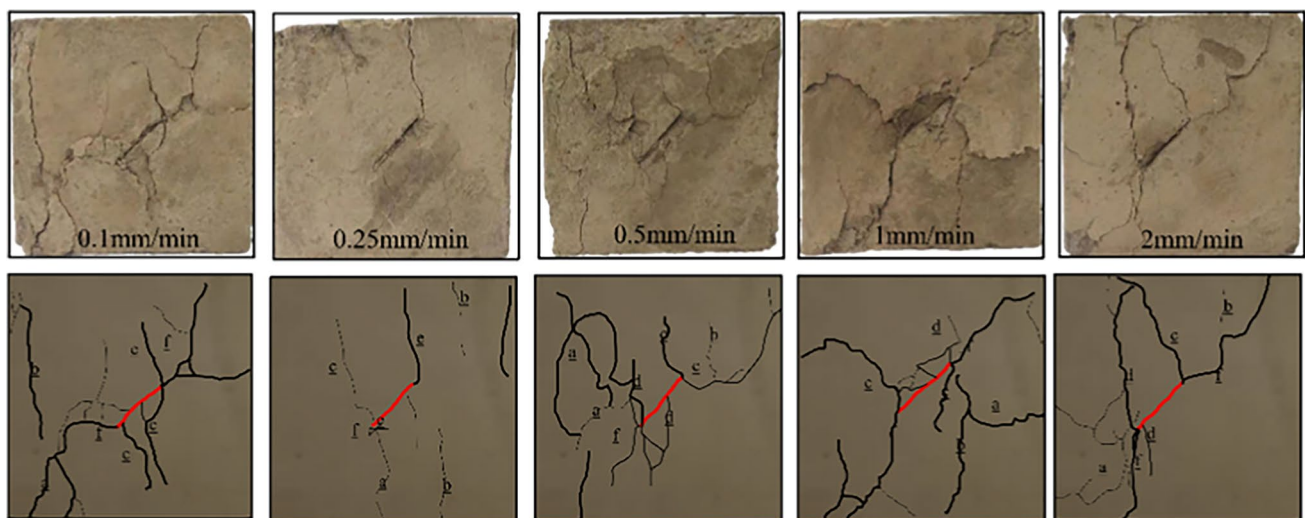


Fig. 9 Failure mode of the filling body (the effect of LR)

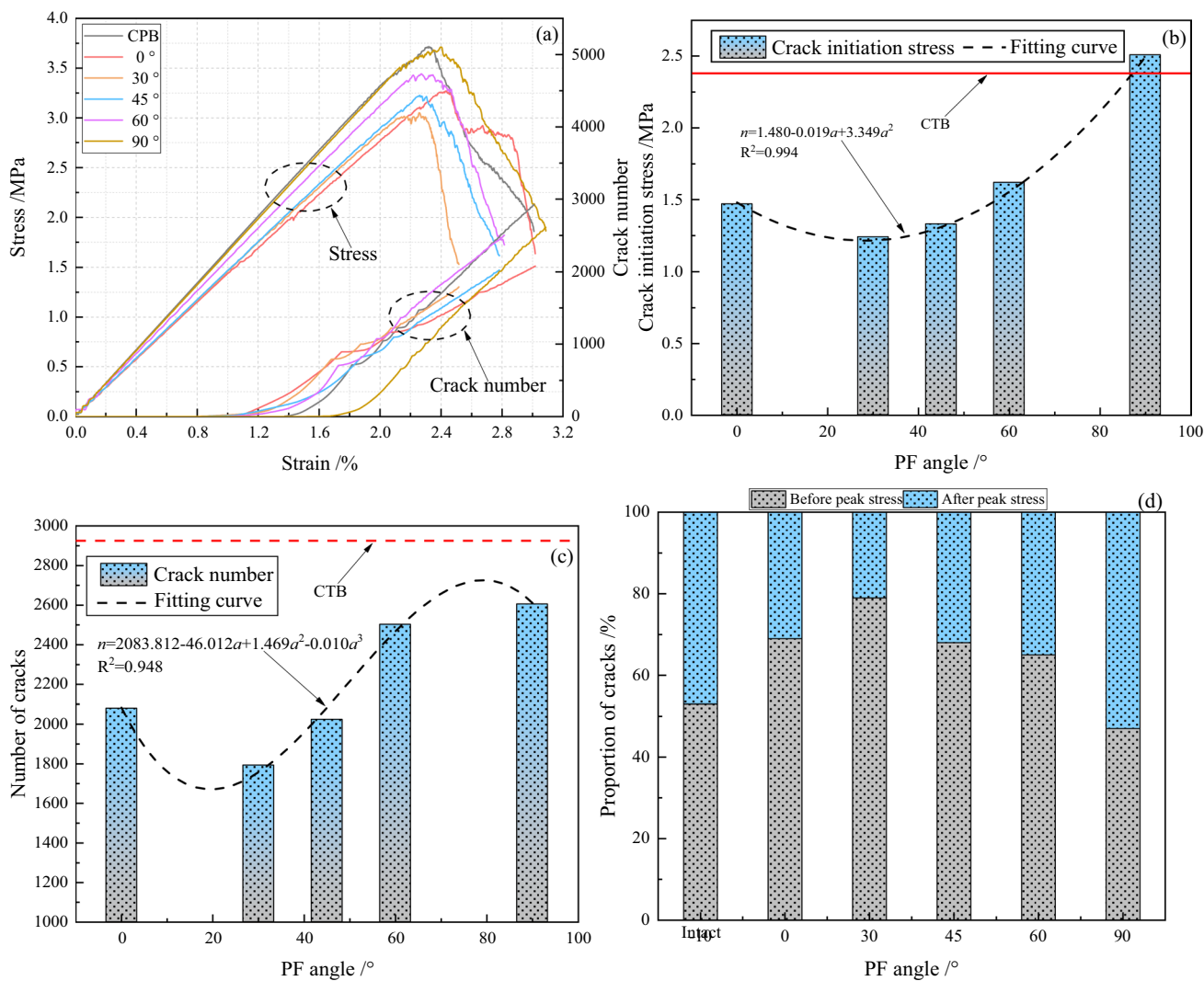


Fig. 10 Mesoscopic crack evolution (the effect of PF angle)

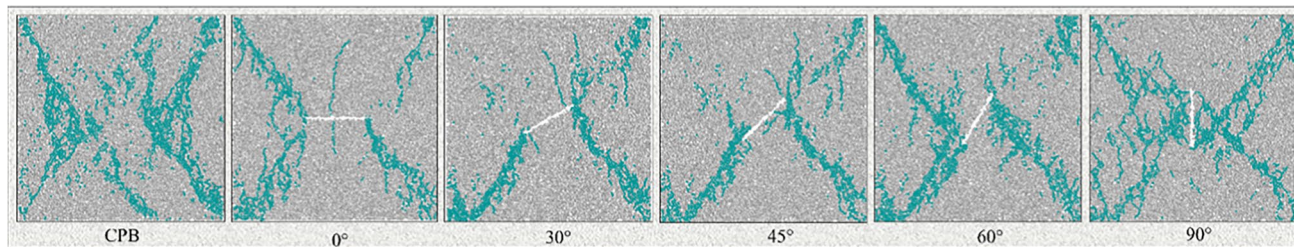


Fig. 11 Mesoscopic failure characteristics of the filling body

phase and reduction crack number. To verify the above analysis, the percentage of pre-peak and post-peak cracks is calculated, as shown in Fig. 10d, which is in line with the above analysis results.

The mesoscopic failure modes of the filling body with different PF angles at LR of 1 mm/min are shown in Fig. 11.

From Fig. 11, it can be found that the CPB mainly occurred shear failure, which was similar to the experimental results (Fig. 8). For the PFCPB, the formation of mesoscopic cracks was distributed around the PF, mainly as follows: (1) There were mesoscopic shear cracks at the left and right tips of 0° PF, and mesoscopic tensile crack existed in the middle

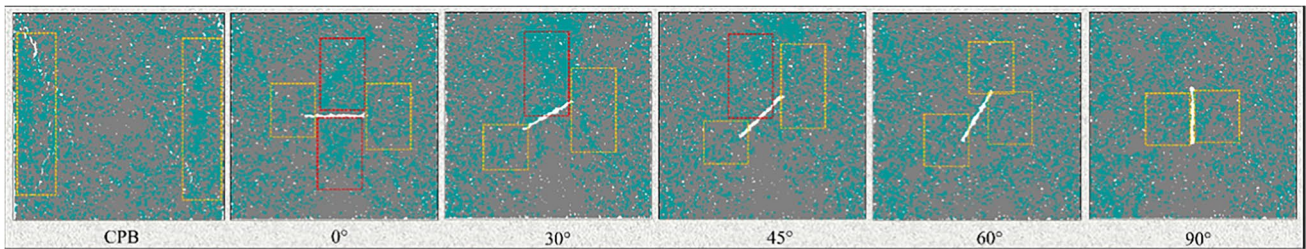


Fig. 12 Distribution of force chain

part above and below the PF respectively. (2) There were mesoscopic shear cracks and tensile cracks at the tip of 30° PF. The mesoscopic crack forms of 45° and 60° PFCPB were similar to those of the 30°PFCPB. (3) When the PF angle increased to 90°, the crack forms were significantly different, which was mainly manifested in that the crack first sprouted on both sides of the PF and extended outward. Figure 12 shows the force chain distribution of different PFCPBs (green represented tensile, gray represented compression). From Fig. 12, It can be found that the tensile force distribution of CPB was more uniform. However, the tensile force inside PFCPB was distributed around the PF. As the PF angle increased, the tensile force concentration on the top and bottom of PF gradually weakened, and the tensile force concentration on the top and bottom of the 0° and 30° PFs was larger, which made the crack more likely to initiate, corresponding to a lower crack initiation stress. There was tension concentration on both sides of the 90° PF, and there was no tension distribution at the two tips. Therefore, the deterioration degree of mechanical properties of 90° PFCPB

was not obvious. The transfer of force chains with PF angle is in agreement with the numerical simulation results gained by Yu et al (2021).

The effect of LR

Uniaxial compression simulations at LRs of 0.1 and 1 mm/min were carried out with a 45° PFCPB, and the results are shown in Fig. 13. From Fig. 13a, it can be clearly found that the number of cracks after mesoscopic damage of 45° PFCPB increased from 1653 at LR of 0.1 mm/min to 2025 at LR of 2 mm/min. Meanwhile, the failure time of the filling body was shortened and the crack initiation was advanced. This is because higher LR corresponded to greater energy input, which promoted earlier crack initiation within the specimen. However, there was a certain hindering effect on crack expansion due to higher LRs (Yu et al. 2021; Gan et al. 2016); more energy was stored inside the specimen before the peak. After the peak, the crack sprouting and propagation rate was rapidly increased and the crack number was higher inside the specimen, while the lower LRs were the

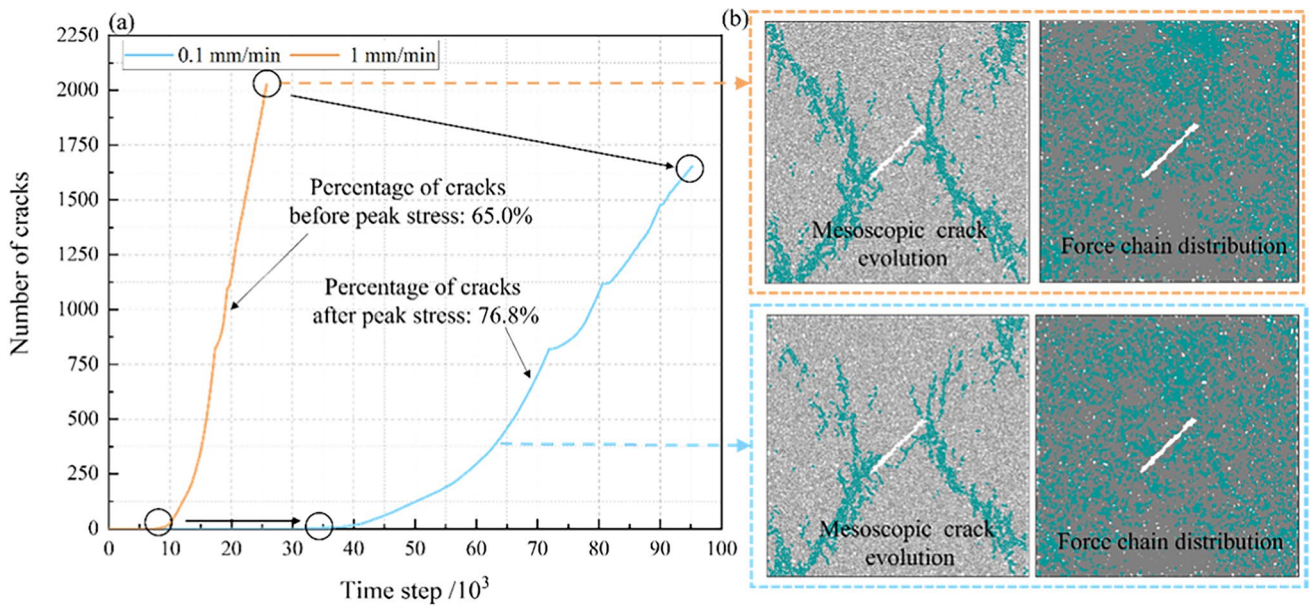


Fig. 13 Mesoscopic crack evolution (the effect of LR)

opposite. According to the statistics of the percentage of pre-peak cracks in Fig. 10d, the percentage of pre-peak cracks at the LR of 0.1 and 1 mm/min was 76.8 and 65.0%, respectively, which further proved the reliability of the above analysis.

As shown in Fig. 13b, the distribution of force chain inside the filling body was changed due to the change of LR, and the cracks generated at both tips of PF were slightly different. Overall, the LR had little effect on the mesoscopic crack propagation characteristics of these samples, which corresponded to the macroscopic failure morphology of PFCPBs shown in Fig. 9.

Mesoscopic AE characteristics of CPB and PFCPB

AE events number

The (mesoscopic) AE event rate and cumulative AE event number of the specimen can be gained according to the

statistics of crack location and moment tensor theory. As can be seen from Figs. 14 and 15:

AE events experience four phases: quiet period, slow rising period, rapid rising period, and rapid falling period. During indoor uniaxial compression, AE events almost accompany the whole loading process. In the initial loading phase, only a limited number of AE events were produced, while the peak of AE events occurred near the peak stress (Fig. 15a). On the contrary, the numerical simulation results showed that no mesoscopic AE events were generated in the initial phase. In addition, the maximum values of AE events were located behind the peak. These phenomena can be explained as follows: (1) There are a large number of defects such as micro-pores and micro-cracks in CPB formed by artificial pouring. In the early stage of loading, these defects were compressed and closed, leading to a small number of AE events. However, the mesoscopic model does not have the abovementioned initial defects,

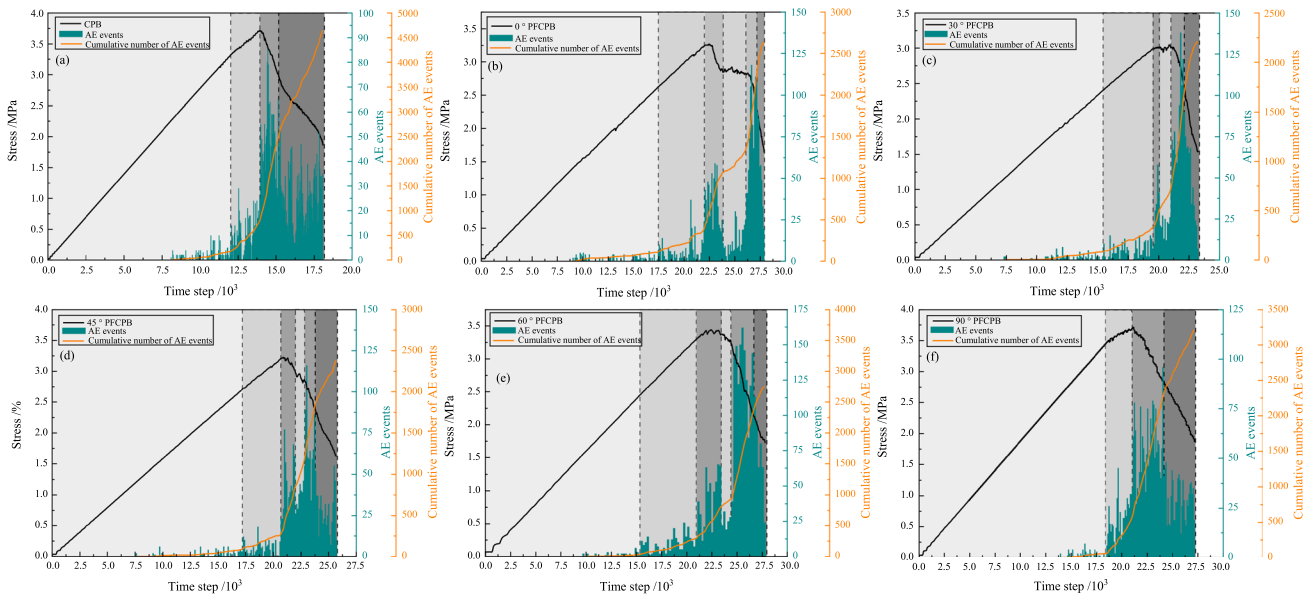


Fig. 14 AE characteristics of the filling body (the effect of PF angle)

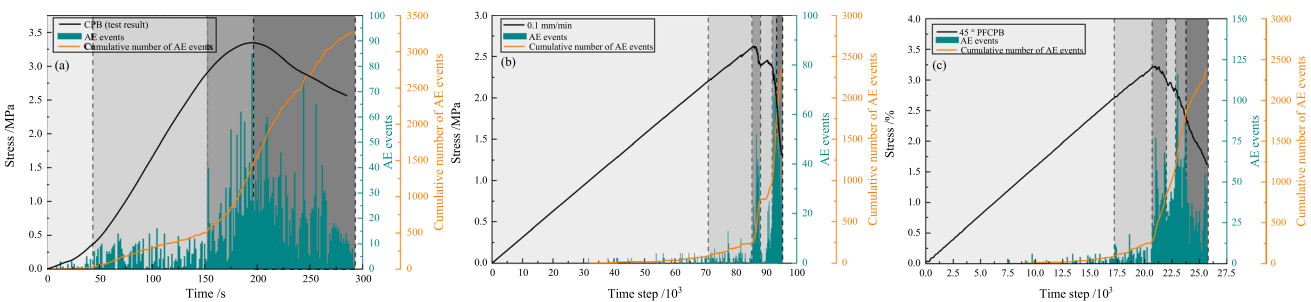


Fig. 15 AE characteristics of the filling body (the effect of LR).

which means that no AE events occur at this stage. (2) Due to data processing or test instrument monitoring problems, AE data captured during the test monitoring may be delayed, resulting in maximum AE events concentrated near the peak stress (Cheng et al. 2021). On the whole, the experimental results were in high agreement with the numerical simulation results, which proved the reliability of mesoscopic AE simulation. The numerical simulation results of AE events obtained in this paper are similar to those of Zhao et al. (2021) and Cheng et al. (2019).

Moreover, the AE event-time step development trend of CPB and 90° PFCPB (Fig. 14a and f) was similar. After the peak stress, the AE events surged, the cracks were rapidly initiated and expanded, and large mesoscopic cracks were formed, resulting in destabilization of the filling body. This phenomenon indicates that the presence of 90° PF has less effect on the crack evolution of PFCPB, and thus, the degree of mechanical property deterioration induced by the PF was reduced, which was in line with the macroscopic test results. Meanwhile, AE events of 0~60° PFCPB appear in advance, which represented the early initiation of cracks (consistent with Fig. 10). It shows that AE events are closely related to crack extension, which is in line with the macroscopic test results. Furthermore, the AE events of these types of PFCPBs undergo two slow rising periods and two rapid rising periods as loading continues. This phenomenon can be explained as follows: the filling body sample is always in the state of energy storage and dissipation before failure. The stress concentration around the 0~60° PFs is more likely to occur, the crack is easier to initiate, and the energy storage capacity of the filling body is reduced, resulting in more energy dissipation in the first rapid rising period of the AE events. Under the subsequent load, the crack growth rate is slowed down, and the AE events are reduced and increased slowly. According to the evolution law of AE events, the rapid rising period of the first AE events can be regarded as the failure precursor of the 0~60° PFCPB. The results are in line with the test results of Song et al. (2022b).

As shown in Fig. 15b–c, compared with the high LR of 1 mm/min, the AE events corresponding to the low LR of 0.1 mm/min appeared later, AE event number was less overall, and the AE quiet period and slow rising period were not significant. However, on the whole, the development trend of AE events under different LRs was similar, and there were two slow rising periods and two rapid rising periods of AE events. This phenomenon further confirmed that the LR has less influence on the crack evolution mode of PFCPBs but mainly controlled the crack evolution rate.

TSD characteristics of AE events

Figure 16 shows the TSD characteristics of AE events for CPB and 0, 30, and 90° PFCPB (LR is 1 mm/min). Figure 17

presents the TSD characteristics of AE of 45° PFCPB under the LR of 0.1 and 1 mm/min. To facilitate the characterization of the time-dependent properties of AE events, the AE event evolution characteristics are analyzed at 80 and 90% of the peak stress, at the peak stress, and at the end position. The TSD characteristics of AE events are discussed in detail below.

It is clear from Fig. 16 that, on the whole, the AE event evolution of CPB and PFCPB was consistent with the crack development, and this phenomenon further supported the close correlation between cracks and AE events. However, the existence of PF inevitably led to changes in the internal stress state of the filling body samples and differences in the form of crack extension, prompting significant differences in the AE events number, magnitude size, and spatial location at different time steps. The main manifestations were as follows: (1) At 80% of the peak stress, there were only a few randomly distributed weak AE events in CPB and 90° PFCPB. AE events in 0° PFCPB were mainly concentrated in the upper and lower part of the middle of the PF, and dense zones of AE events were formed. In contrast, the AE events in the 30° PFCPB were mainly concentrated in the PF tip, and there were more AE events with larger magnitude. (2) When the loading continued to 90% of the peak stress, the AE events increased slightly at each working condition. AE events remained low for CPB and 90° PFCPB. AE events of 0° PFCPB increased at the PF tip, while the 30° PFCPB had more AE events at the right tip of PF and was accompanied by larger magnitude AE events. (3) When the filling body reached the peak stress, the AE events of all backfill samples increased significantly. AE event concentration zone appeared on both sides of CPB, while the AE events of 90° PFCPB were concentrated on the side of PF. The CPB and 90° PFCPB were still dominated by minor AE events. However, numerous AE events were produced at the PF tips of 0° and 30° PFCPBs, especially the dense AE concentration zone had been formed at the upper and lower tips of the 30° PF, and AE events with large magnitude occurred frequently. It indicates that the cracks inside the filling body sprout and expand rapidly, and the degree of damage is larger. (4) In the post-peak stage, the crack expanded rapidly, and numerous AE events and AE events with larger magnitude appeared rapidly. The AE events of PFCPB still develop to both sides with the PF as the center, or the surrounding AE events gathered to the PF, which corresponded to the crack development pattern of the filled body. The phenomenon of a rapid increase in post-peak AE events for CPB and 90° PFCPB is consistent with the pre-peak and post-peak crack proportions.

It can be seen from Fig. 17 that at 80 and 90% of the peak stress, fewer AE events were mainly distributed at the tip of PF, and there were relatively more AE events in the filling body when the LR was 1 mm/min. When the peak stress

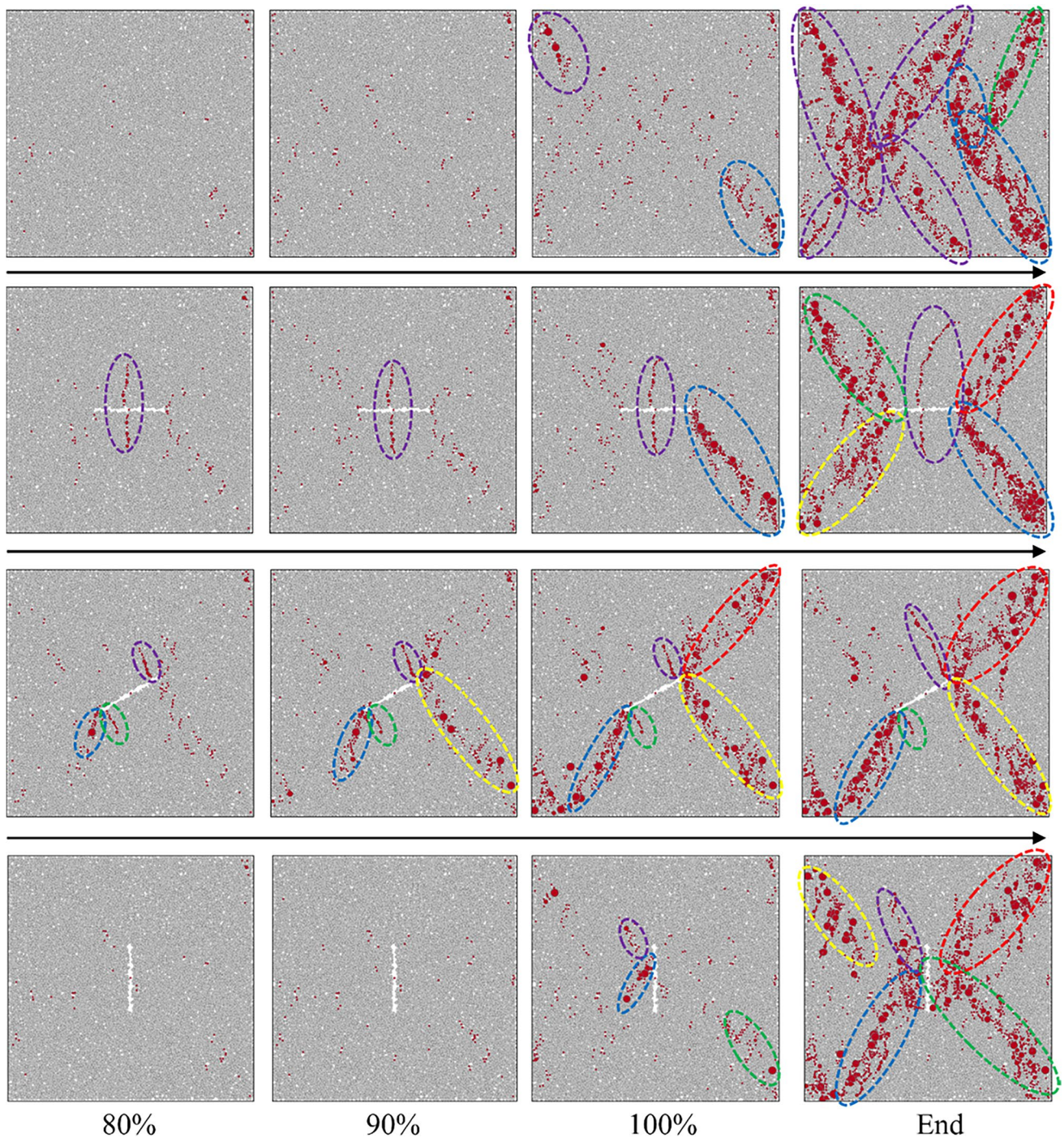


Fig. 16 TSD characteristics of AE events (the effect of PF)

was reached, AE events (AE events with larger magnitude) increased rapidly, dense AE event concentration zones appeared along the PF tip, and there were more AE event concentration zones at LR of 1 mm/min. In the post-peak stage, AE events increased sharply, AE events with larger magnitude occurred frequently, multiple dense zones were formed, and the filling body was unstable and damaged.

Discussion

The instability and failure of rock, concrete, and filling materials under external loads are essentially a progressive damage evolution process driven by energy, which is a comprehensive manifestation of the closure, development, expansion, and penetration of internal micro-cracks

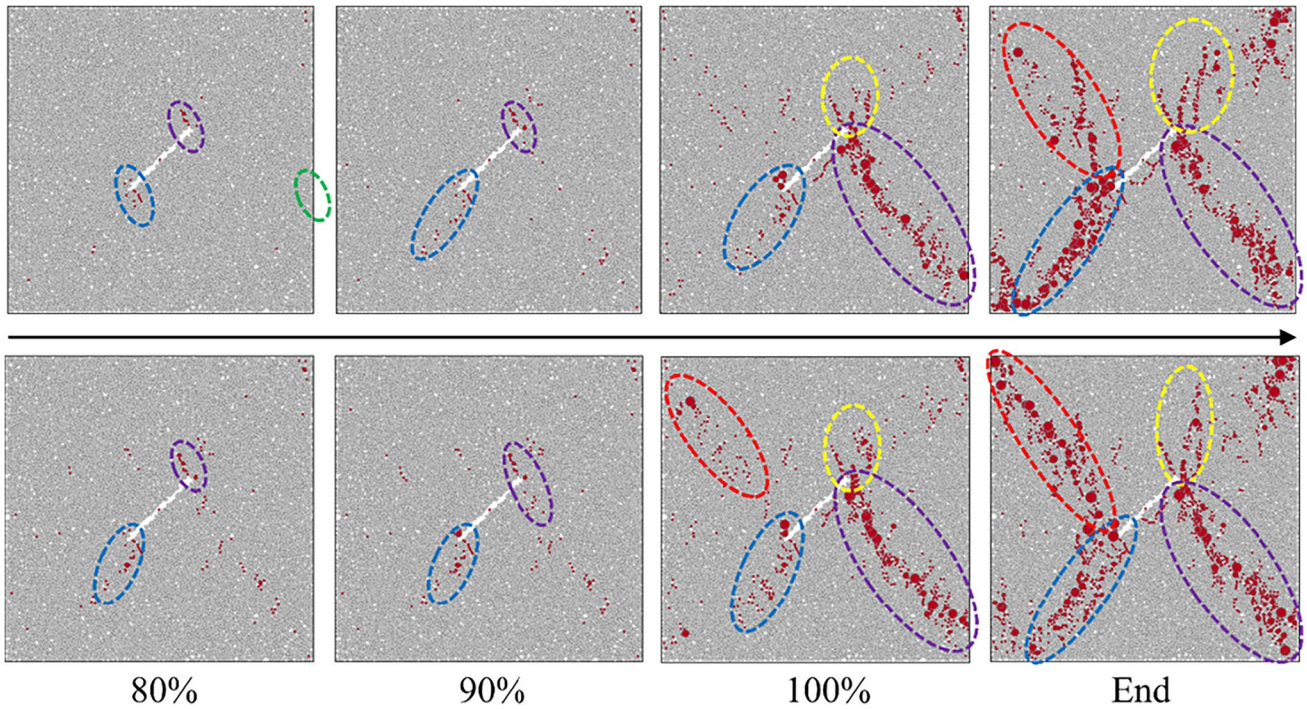


Fig. 17 TSD characteristics of AE (the effect of LR)

(Wang et al. 2021a, b; Liu et al. 2020). The change of PF angle and LR will inevitably lead to the difference of energy exchange in the whole test process, which in turn induced significant changes in the crack evolution characteristics and mechanical properties inside the filling body, resulting in the obvious difference of AE events source. Therefore, the energy evolution law of PFCPB based on PFC2D was analyzed to reveal the PF deterioration mechanism and LR effect of the filling body from the energy perspective.

Assuming that the energy exchange between the filling body and the outside world during the test is not considered, the work done by the load on the filling body is (Zhao et al. 2021; Liu et al. 2020):

$$U_b = U_e + U_d \tag{10}$$

where U_b is the boundary energy; U_e is the strain energy; U_d is the dissipation energy.

In the numerical simulation of PFC, the boundary energy is derived from the work done by the upper and lower walls. The strain energy includes the strain energy of the particles themselves (U^s) and the strain energy of the parallel bond model (U^{ep}); the dissipation energy includes the damping energy (U^d), slip energy (U^{sl}), and kinetic energy (U^k) between the particles and is calculated as follows (Zhao et a. 2021):

$$\begin{cases} U_e = U_s + U_p \\ U^s = \frac{1}{2} \left[\frac{(F_n^1)^2}{k_n} + \frac{\|F_s^1\|^2}{k_s} \right] \\ U^{ep} = \frac{1}{2} \left(\frac{\bar{F}_n^2}{k_n \cdot \bar{A}} + \frac{\|F_n\|}{k_s \cdot \bar{A}} + \frac{\bar{M}_t^2}{k_s \cdot \bar{J}} + \frac{\|\bar{M}_b\|^2}{k_s \cdot \bar{I}} \right) \end{cases} \tag{11}$$

where F_n^1 , F_s^1 , \bar{F}_n , and \bar{F} are the normal and tangential contact forces between the linear contact and parallel bonded contact between particles, respectively; k_n , k_s , \bar{k}_n , and \bar{k}_s are the normal and tangential stiffness between the linear contact and parallel-bonded contact between particles, respectively. M_t is the torque of parallel bonding contact; \bar{M}_b is the bending moment of parallel bond contact; \bar{A} is the contact area; \bar{J} is the polar moment of inertia; \bar{I} is the moment of inertia of the contact.

The results of each energy statistic of CPB and PFCPB in the uniaxial compression process are shown in Table 3 and Fig. 18. It can be seen from Fig. 18a that the energy values of CPB were much higher than those of PFCPB. This is because the integrity of the filling body was decreased by the presence of PF, the crack initiation stress of the filling body was weakened, resulting in the reduction of the energy storage limit of the filling body. Moreover, the higher dissipation energy of CPB can be attributed to the fact that more energy is stored in the pre-peak phase and more energy is

dissipated in the post-peak phase, which will also induce numerous cracks to be sprouted and the crack extension and propagation to be accelerated. Simultaneously, with the increase of PF angle, each energy value first decreased slightly and then increased gradually. The strain energy and dissipation energy of PFCPB decreased slightly from 3.93 and 2.16 kJ/m³ at 0° to 3.87 and 2.12 kJ/m³ at 30° and then gradually increased to 4.60 and 2.57 kJ/m³ at 90°. This phenomenon further indicated that the energy evolution of the filling body is influenced by the PF and PF angle, and thus, the mechanical behavior of the filling body is altered. The energy storage capacity of 30° PFCPB is the smallest. When the PF angle gradually increased from 30 to 90°, the effect of PF on the energy storage capacity of filling body gradually decreased. The energy evolution is in line with the mechanical properties of PFCPB, which shows that the energy evolution law obtained by numerical simulation can be used to explain the evolutionary characteristics of the mechanical behavior of PFCPB.

As shown in Fig. 18b, the boundary energy, strain energy, and dissipation energy of the 45° PFCPB were rapidly increased from 3.46, 2.26 and 1.20 kJ/m³ at LR of 0.1 mm/min to 6.29, 4.01, and 2.26 kJ/m³ at LR of 1 mm/min, respectively. This result further verified that the interpretation of the effect of LR on the mechanical properties of the filling body in the “Results and analysis” and “The mesoscopic characteristics of CPB and PFCPB” sections is correct, i.e., increasing the LR correspondingly increases the external energy input (corresponding to an increase in the boundary energy), and the higher energy input induces the filling body to consume some of the energy in the form of increasing its stress. Meanwhile, the higher strain energy accumulation before the peak is bound to cause the rapid increase of dissipation energy after the peak, and the crack sprouts and expands rapidly. This phenomenon is in line with the crack evolution law and AE characteristics in the “The mesoscopic characteristics of CPB and PFCPB” section.

Table 3 Energy evolution law of the filling body under different conditions

Energy (kJ/m ³)	PF angle /°						LR (mm/min)	
	CPB	0	30	45	60	90	0.1	1
U _d	0.17	0.18	0.17	0.18	0.19	0.21	0.09	0.18
U _k	0.21	0.16	0.13	0.11	0.20	0.20	0.04	0.11
U _{ep}	3.33	2.67	2.65	2.69	2.89	2.93	1.63	2.69
U _{sl}	2.31	1.82	1.82	1.99	2.11	2.17	1.08	1.99
U _s	1.90	1.26	1.22	1.32	1.41	1.67	0.63	1.32
U _e	5.23	3.93	3.87	4.01	4.30	4.60	2.26	4.01
U _d	2.69	2.16	2.12	2.28	2.39	2.57	1.20	2.28
U _b	7.92	6.09	5.99	6.29	6.69	7.17	3.46	6.29

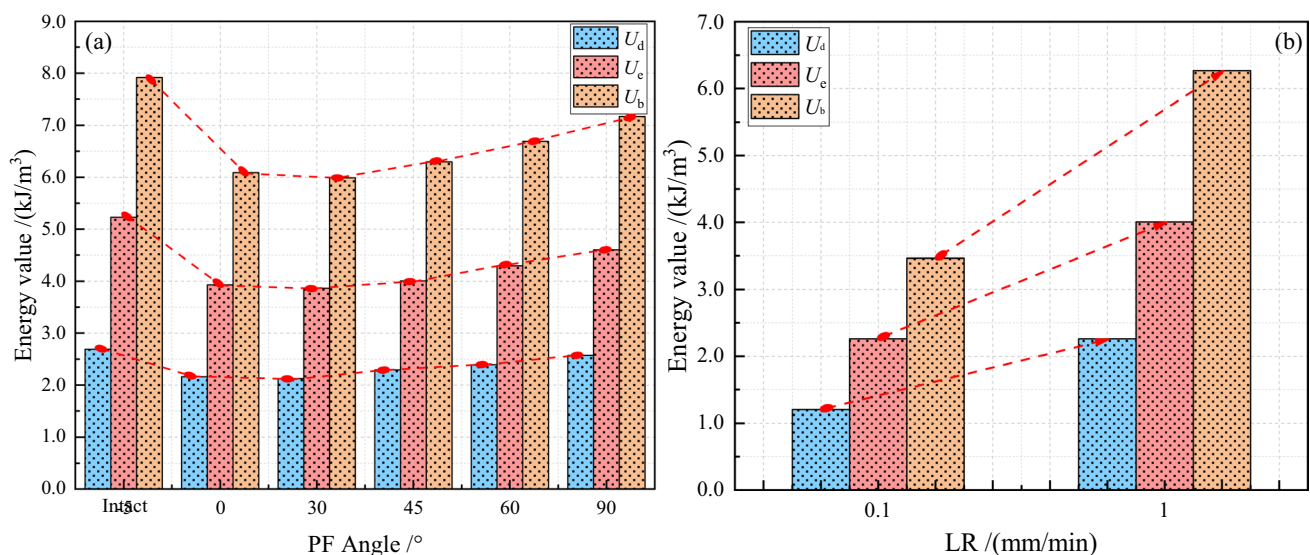


Fig. 18 Energy value of the filling body under different conditions

Conclusions

In this study, the mechanical properties, failure mode, mesoscopic AE characteristics, and energy exchange law of CPB and PFCPB under different LRs were obtained by combining experimental test and numerical simulation. The main conclusions are as follows:

- (1) The mechanical behavior of the filling body was deteriorated by the PF. The UCS and EM increased and then decreased with the enhancement of the PF angle; 30° PF had the most significant effect. The filling body had an obvious LR effect, and UCS and EM were positively correlated with LR.
- (2) The stress–strain curves of the filling body (90° PFCPB and CPB) were similar to the traditional curves, and both went through four stages. However, in the process of loading, the top and bottom parts of PF were closed, and the stress fluctuated greatly. The stress–strain curve of 0~60° PFCPB continued to rise after varying degrees of stress drop in the pre-peak or post-peak stage due to the PF angle and LR.
- (3) PFC2D simulation shows that the crack initiation stress of the filling body was decreased by the PF. During the loading process, the crack initiated and propagated around the PF. When the LR increased from 0.1 to 1 mm/min, the number of cracks of 45° PFCPB increased from 1653 to 2025 after mesoscopic failure, the failure time was shortened, and the crack initiation was advanced.
- (4) The AE events of CPB and the 90° PFCPB all experienced quiet, slow rising, rapid rising, and rapid falling periods. However, the AE events of 0~45° PFCPB experienced two slow rising periods and two rapid rising periods. Furthermore, the TSD characteristics of AE events indicated that the presence of PF (except 90°) and the increase of LR promoted the occurrence of AE events in advance, and AE events with larger magnitudes occur frequently.
- (5) The energy storage capacity of the filling body was decreased by the presence of PF, and the crack was easily generated around the PF. The higher strain energy before the peak caused the energy to be rapidly dissipated after the peak, and the crack was rapidly sprouted and expanded. The energy value of the filling body was positively correlated with the LR. The higher LR increased the energy input, which urged the filling body to consume part of the energy by improving its stress ability, and the higher LR had a certain blocking effect on the crack propagation, which was conducive to the improvement of the mechanical properties of the filling body.

In this paper, the influence of prefabricated fracture and loading rate on the mechanical properties of the filler was investigated by a combination of experiments and numerical simulations, and the crack-cracking mechanism was revealed. In the actual filling mining operation, a reasonable recovery rate is essential to ensure the stability of the backfill. Meanwhile, monitoring and protection of the filling body with initial cracks due to blasting disturbance should be strengthened, especially cracks with 0~45° on the surface of the filling body. Furthermore, the prefabricated fractures of PFCPB prepared in this paper are penetration fractures, and only UCS tests have been carried out. In future work, it is important to consider the depth of prefabricated fracture embedded inside the filling body, and creep tests should be conducted.

Author contribution Xuepeng Song: conceptualization, supervision, visualization, project administration writing—review and editing, experiments, data curation. Quan Yuan: conceptualization, supervision, writing—review and editing. Shi Wang: conceptualization, supervision, writing—review and editing, co-ordination and funding acquisition. Zilin Dong: conceptualization, supervision. Yuxin Hao: data curation, experiments.

Funding This work received financial support provided by the National Natural Science Foundation of China (No. 51804134). The Program of Qingjiang Excellent Young Talents, Jiangxi University of Science and Technology (JXUSTQJYX2019007).

Data availability The datasets used and/or analyzed during the current study are available from the corresponding author on reasonable request.

Declarations

Ethics approval and consent to participate. Not applicable.

Consent for publication Not applicable.

Conflict of interest The authors declare no competing interests.

References

- Cao RH, Cao P, Fan X, Xiong X, Lin H (2016) An experimental and numerical study on mechanical behavior of ubiquitous-joint brittle rock-like specimens under uniaxial compression. *Rock Mech Rock Eng* 49(11):4319–4338
- Cao S, Yilmaz E, Song WD, Yilmaz E, Xue GL (2019) Loading rate effect on uniaxial compressive strength behavior and acoustic emission properties of cemented tailings backfill. *Constr Build Mater* 213:313–324
- Cheng AP, Zhang YS, Wang P, Dai SY, Dong FS (2019) Strain rate and acoustic emission characteristic response law of cemented backfill. *J Harbin i Technology* 51(10):130–136
- Cheng AP, Shu PF, Deng DQ (2021) Microscopic acoustic emission simulation and fracture mechanism of cemented tailings backfill based on moment tensor theory. *Constr Build Mater* 308:125069

- Fang K, Fall M (2018) Effects of curing temperature on shear behaviour of cemented paste backfill rock interface. *Int J Rock Mech Min Sci* 112:184–192
- Gan DQ, Han L, Liu ZY, Zhao HX (2016) Experimental study of the effect of loading rate on strength performance of filling body. *Met Min* 12:150–153
- Haeri H, Shahriar K, Marji MF, Moarefvand P (2014) Experimental and numerical study of crack propagation and coalescence in pre-cracked rock-like disks. *Int J Rock Mech Min Sci* 67:20–28
- Harizi W, Chaki S, Bourse G, Ourak M (2022) Damage mechanisms assessment of glass fiber-reinforced polymer (GFRP) composites using multivariable analysis methods applied to acoustic emission data. *Compos Struct* 289:115470
- He ZW, Zhao K, Yan YJ (2021) Mechanical response and acoustic emission characteristics of cement paste backfill and rock combination. *Constr Build Mater* 288:123119
- Hou JF, Guo ZP, Liu WZ, Zhang YX (2020a) Mechanical properties and meso-structure response of cemented gangue-fly ash backfill with cracks under seepage- stress coupling. *Constr Build Mater* 250:118863
- Hou YQ, Yin SH, Cao Y, Dai CQ (2020b) Research on damage and energy dissipation characteristics of cemented backfill under different loading rates. *J Hunan U Natural SC* 47(8):108–117
- Hou C, Yang LJ, Li L, Yan BX (2022) Mechanical characteristics and stress evolution of cemented paste backfill: effect of curing time, solid content, and binder content. *Front Mater* 8:812402
- Hu XJ, Bian K, Liu J, Chen M, Cen Y, Liu ZP (2021) Particle flow simulation of the influence of granite crystal size distribution on acoustic emission characteristics. *J China Coal Soc* 46(s2):721–730
- Huang Z, Gu QX, Wu YF, Wu Y, Li SJ, Zhao K, Zhang R (2021) Effects of confining pressure on acoustic emission and failure characteristics of sandstone. *Int J Min Sci Technol* 31:963–974
- Huang YH, Yang SQ, Tian WL, Wu SY (2022) Experimental and DEM study on failure behavior and stress distribution of flawed sandstone specimens under uniaxial compression. *Theor Appl Fract Mech* 118:103266
- Khazaei C, Hazzard J, Chalaturnyk R (2015) Damage quantification of intact rocks using acoustic emission energies recorded during uniaxial compression test and discrete element modeling. *Comput Geotech* 67:94–102
- Kuyuk AF, Ghoreishi-Madiseh SA, Hassani FP (2020) Closed-loop bulk air conditioning: a renewable energy-based system for deep mines in arctic regions. *Int J Min Sci Technol* 30:511–516
- Li BX, Song Y, Yang L, Zhu WS, Xue YG, Feng D, Wang C, Chen YJ (2022) Multiscale fracture characteristics and failure mechanism quantification method of cracked rock under true triaxial compression. *Eng Fract Mech* 262:108257
- Liu WL, Yan EC, Dai H (2020) Study on characteristic strength and energy evolution law of Badong formation mudstone under water effect. *Chin J Rock Mech Eng* 39(2):311–326
- Lu R, Ma FS, Zhao J, Guo J, Gu JZ, Huang YQ (2021) Analysis of acoustic emission index characteristics for indoor uniaxial compression test of backfill. *Gold Sci Technol* 29(2):217–224
- Ma J, Wu SC, Zhang XP, Gan YX (2020) Modeling acoustic emission in the Brazilian test using moment tensor inversion. *Comput Geotech* 123:103567
- Mondoringin MRIAJ, Ohtsu M (2013) Kinematics on split-tensile test of fiber reinforced concrete by AE. *J Adv Concr Technol* 11(8):196–205
- Shimbo T, Shinzo C, Uchii U, Itto R, Fukumoto Y (2022) Effect of water contents and initial crack lengths on mechanical properties and failure modes of pre-cracked compacted clay under. *Eng Geol* 301:106593
- Shirole D, Hedayat A, Gabriel W (2021) Damage monitoring in rock specimens with pre-existing flaws by non-linear ultrasonic waves and digital image correlation. *Int J Rock Mech Min Sci* 142:104758
- Song XP, Hao YX, Wang S, Zhang L, Liu HB, Yong FW, Dong ZL, Yuan Q (2022a) Dynamic mechanical response and damage evolution of cemented tailings backfill with alkalinized rice straw under SHPB cycle impact load. *Constr Build Mater* 327:127009
- Song XP, Hao YX, Wang S, Zhang L, Liu W, Li JB (2022b) Mechanical properties, crack evolution and damage characteristics of prefabricated fractured cemented paste backfill under uniaxial compression. *Constr Build Mater* 330:127251
- Sun W, Wu SC (2021) A study of crack initiation and source mechanism in the brazilian test based on moment tensor. *Eng Fract Mech* 246:107622
- Tang YJ, Hao TX, Li F, Zhao LZ, Liu J (2022) Energy evolution and infrared radiation characterization of coal rocks considering strain rate effect. *Chin J Rock Mech Eng* 41:1–11
- Tao J, Yang XG, Ding PP, Li XL, Zhou JW, Lu GD (2022) A fully coupled thermo-hydro-mechanical-chemical model for cemented backfill application in geothermal conditions. *Eng Geol* 302:106643
- Wang CL, Du GY, Li EB, Sun X, Pan Y (2021a) Evolution of strength parameters and energy dissipation of Beishan deep granite under conventional triaxial compression. *Chin J Rock Mech Eng* 40(11):2238–2248
- Wang S, Song XP, Wei ML, Liu W, Wang XJ, Ke YX, Tao TJ (2021b) Strength characteristics and microstructure evolution of cemented tailings backfill with rice straw ash as an alternative binder. *Constr Build Mater* 297:123780
- Wang AA, Cao S, Yilmaz E (2022a) Influence of types and contents of nano cellulose materials as reinforcement on stability performance of cementitious tailings backfill. *Constr Build Mater* 344:128179
- Wang J, Li JT, Shi ZM (2022b) Deformation damage and acoustic emission characteristics of red sandstone under fatigue–creep interaction. *Theor Appl Fract Mech* 117:103192
- Wu Y, Huang Z, Zhao K, Zeng W, Gu QX, Zhang R (2020) Unsteady seepage solutions for hydraulic fracturing around vertical wellbores in hydrocarbon reservoirs. *Int J Hydrogen Energy* 45:9496–9503
- Xie HP (2019) Research review of the state key research development program of China: deep rock mechanics and mining theory. *J China Coal Soc* 44(5):1283–1305
- Xin J (2020) Experimental investigation on microstructure, mesostructure and mechanical properties of cemented paste backfill. Master's Thesis, Xi'an Univ Sci Technol 1–60
- Xiu ZG, Wang SH, Jing YC, Wang FL, Ren FY, Nguyen VT (2021) Loading rate effect on the uniaxial compressive strength (UCS) behavior of cemented paste backfill (CPB). *Constr Build Mater* 271:121526
- Xu WB, Wan CB, Tian XC (2018) Coupling effect of temperature and fracture on the strength and crack propagation mode of backfill mass. *J Min Saf Eng* 35(3):612–619
- Xue Y, Ranjith PG, Chen Y, Cai CZ, Gao F, Liu XG (2023) Nonlinear mechanical characteristics and damage constitutive model of coal under CO₂ adsorption during geological sequestration. *Fuel* 331:125690
- Yilmaz E (2018) Stope depth effect on field behaviour and performance of cemented paste backfills. *Int J Rock Mech Min Sci* 32(4):273–296
- Yu H, Liu SW, Jia HS (2020) Mechanical response and energy dissipation mechanism of closed single fracture sandstone under different confining pressures. *J Min Saf Eng* 37(2):385393
- Yu LQ, Yao QL, Xu Q, Wang WN, Niu ZJ, Liu WD (2021) Experimental and numerical simulation study on crack propagation of

- fractured fine sandstone under the influence of loading rate. *J China Coal Soc* 41(11):3488–3501
- Zhang S, Wu S, Zhang G, Guo P, Chu C (2020) Three-dimensional evolution of damage in sandstone Brazilian discs by the concurrent use of active and passive ultrasonic techniques. *Acta Geotech* 15(2):393–408
- Zhang H, Cao S, Yilmaz E (2022) Influence of 3D-printed polymer structures on dynamic splitting and crack propagation behavior of cementitious tailings backfill. *Constr Build Mater* 343:128137
- Zhao K, Yu X, Zhou Y, Wang Q, Wang JQ, Hao JL (2020a) Energy evolution of brittle granite under different loading rates. *Int J Rock Mech Min Sci* 132:104392
- Zhao K, Yu X, Zhu ST (2020b) Acoustic emission fractal characteristics and mechanical damage mechanism of cemented paste backfill prepared with tantalum niobium mine tailings. *Constr Build Mater* 258:119720
- Zhao K, Liu YG, Zeng P, Wu WK, Wang JJ (2021) Study on the acoustic emission characteristics of granite in relative calm period based on GBM model of particle flow code. *Met Min* 543(9):27–36
- Zhao ZY, Cao S, Yilmaz E (2022a) Effect of layer thickness on flexural property and microstructure of 3D printed rhomboid polymer reinforced cemented tailings composites. *Int J Miner Metall Mater* 1–27
- Zhao ZY, Guo KH, Wang XL (2022b) A binder prepared by low-reactivity blast furnace slags for cemented paste backfill: influence of super-fine fly ash and chemical additives. *Constr Build Mater* 327:126988

Publisher's note Springer Nature remains neutral with regard to jurisdictional claims in published maps and institutional affiliations.

Springer Nature or its licensor (e.g. a society or other partner) holds exclusive rights to this article under a publishing agreement with the author(s) or other rightsholder(s); author self-archiving of the accepted manuscript version of this article is solely governed by the terms of such publishing agreement and applicable law.